Available online at www.sciencedirect.com

ScienceDirect

journal homepage: www.elsevier.com/locate/bbe

Original Research Article

Understanding the interplay between baroreflex gain, low frequency oscillations, and pulsatility in the neural baroreflex

John V. Ringwood *, *Hasana Bagnall-Hare*

Dept. of Electronic Engineering, Maynooth University, Maynooth, County Kildare, Ireland

ARTICLE INFO

Article history:
Received 7 April 2020
Received in revised form
15 July 2020
Accepted 16 July 2020
Available online 13 August 2020

Keywords:
Mean arterial pressure
Pulsatility
Low-frequency oscillations
Nonlinear feedback model
Neural baroreflex

ABSTRACT

The neural baroreflex, which regulates mean arterial pressure (MAP) via the action of the brain, consists of baroreceptors which measure MAP, and actuators that can produce a change in MAP, such as the heart and parts of the peripheral resistance containing innervated smooth muscle. The brain is the controlling unit, maintaining an appropriate MAP in spite of various disturbances. Under certain circumstances, including haemorrhage and other states of distress, the gain of the neural baroreflex can change, causing low frequency (LF) oscillations (sometimes termed Mayer waves) in blood pressure (BP). Though their purpose is unclear, the origins of these LF oscillations has previously been explained via a nonlinear feedback model, though focusing on the peripheral resistance as an MAP actuator only. The present paper now includes analytical and simulation results explaining the LF oscillation phenomenon for the full neural baroreflex, containing both peripheral resistance (PR) and cardiac branches. However, the main contribution of the paper is to examine the effect of blood pulsatility, or a lack of pulsatility, on the neural baroreflex, and how it's effect can manifest in the presence of LF oscillations. This may have importance in cases where pulsatility is reduced (for example where left-ventricular assist devices are present), or completely absent (for example in turbine-based artificial hearts).

1. Introduction

The human body displays a variety of oscillatory phenomena, many related to the necessary natural means by which flow (of both air and fluids) can be generated. In particular, the rhythms of respiration and blood flow are well known and understood, though some rhythms are less so, for example the low frequency (LF) oscillations in blood pressure (BP), often termed Mayer waves [1], occurring at roughly 0.1 Hz in humans. It should be noted that the frequency of this LF oscillation is species dependent, occurring at roughly 0.3 Hz in rabbits and 0.4 Hz in rats [2].

Since we use the same inlet and outlet pathway for breath, it makes sense that a reciprocating (oscillating) flow is employed. However, in the case of the closed-cycle circulatory

* *Corresponding author at*: Dept. of Electronic Engineering, Maynooth University, Maynooth, Co. Kildare, Ireland
E-mail address: john.ringwood@mu.ie (J.V. Ringwood).

https://doi.org/10.1016/j.bbe.2020.07.008

system, there is a choice between a turbine-type pump and a pulsatile pump. Pulsatility in blood flow is something that we take for granted in healthy humans and animals, and is an inevitable consequence of nature's relative difficulty in synthesising a turbine-type heart, with Moazami et al. [3] contending that ''evolution has favored a pulsatile heart pump to be able to deliver the maximum flow at different levels of systemic vascular resistance, confer kinetic energy to the flow of blood past areas of stenosis and generate low shear stress on blood elements''. Thus, we may imagine that blood flow (and pressure) pulsatility is an unavoidable 'side effect' of an inability to synthesise a constant-flow pump. However, some evidence now suggests that pulsatility may have an important function in maintaining perfusion to ensure that there is an adequate supply of oxygen and nutrients to vital organs. For example [4] demonstrates that when a subject was dependant on a non-pulsatile heart, the perfusion to a number of capillaries was reduced significantly, but not restored to some capillaries when pulsatility was recovered.

In the case where healthy hearts become diseased or lose some of their pumping potential, patients may be fitted with an artificial heart, or left-ventricular assist device (LVAD). Given the artificial nature of these devices, there is a choice as to the use of pulsatile- or continuous-flow designs. In general, turbine-based models are favoured, motivated by the short lifetime and large abdominal cavity required by comparable pulsatile devices [5]. While the benefits of continuous-flow devices are also demonstrated by improvements in patient outcomes [6], there is still some concern regarding the long term physiological effects of diminished blood flow pulsatility.

To some extent, the effect of LVAD insertion on LF oscillations has been considered in the literature, with Cooley et al. [7] show that the presence of an LVAD significantly increases the presence of LF oscillations in R-R interval. While not specifically addressing the issue of LF oscillations, the studies in [8,9] examine broader aspects of non-pulsatile vs. pulsatile blood flow.

Other models for the neural baroreflex, combining both resistance and cardiac branches have been proposed, but employ different analytical tools, and pursue different objectives. For example, [10] employs cross-recurrence analysis to examine the coupling between heart-rate and vascular sympathetic tone, while [11,12] examine heart-rate variability for chaotic behaviour. The model of [13] is used to examine the effect of disease on cardiovascular autonomic regulation, and [14] examines the haemodynamic response to blood volume perturbations.

The studies in [15] and [16] are among the very few to give consideration to the role of pulsatility within the baroreflex loop. The baroreflex model of Ursino [15] includes a comprehensive circulatory model, with both sides of the heart simulated. It also models heart pulsatility, and provides simulation results and comparative experimental results, but conclusions relating baroreflex characteristics to pulsatility are limited to static loading cases. The study in [16] also considers pulsatility, but models pulsatility simply as a ramp signal, and considers the effect of pulsatility on the baroreflex in a qualitative, rather then quantitative way.

This paper, through the development of a mathematical baroreflex model, combined with analysis techniques from the control sciences, examines the role of pulsatility in moderating the neural baroreflex and, inter alia, shows a relationship between BP pulsatility and LF (Mayer) waves. In particular, the analysis in the paper shows that, with reduced or absent pulsatility, baroreflex gain may significantly *increase* with potential consequences for long-term healthy BP dynamics. The analysis in the paper also shows that the increase in baroreflex gain is also generally accompanied by an increase in incidence of LF oscillations [17], which can potentially be used as a surrogate diagnostic tool for baroreflex gain.

This paper extends the work reported in a number of previous publications, notably [2], which examine the conditions under which LF oscillations take place, but only consider the peripheral resistance (PR) baroreflex. [18] considers both PR and cardiac branches, but ignores both BP pulsatility and arterial compliance. [19] articulates the effect of pulsatility on the baroreflex gain, but uses a simplified model of the baroreflex, containing only the PR loop and also ignores arterial compliance. Finally, [20] includes both cardiac and PR branches, along with pulsatility, but omits arterial compliance. The results in [20] are exclusively simulation based. In contrast, the current paper has a comprehensive model for the neural baroreflex, containing both cardiac and PR branches, includes arterial compliance and pulsatility, and develops an analytical solution for the presence of LF oscillations, which is shown to have a solution consistent with results from computer simulation of the model, and also those determined experimentally [21]. Furthermore, we include an analysis which examines the relative importance of individual cardiac (sympathetic and parasympathetic) branches and peripheral resistance branches in mediating LF oscillations. This is performed both through an analytical sensitivity analysis and simulation.

2. Materials and methods

2.1. *The neural baroreflex*

In essence, the neural baroreflex activates smooth muscle in the peripheral resistance, and modulates heart rate, in response to disturbances in mean arterial pressure (MAP) or metabolic needs. In order to provide a feedback mechanism, BP is measured in the aortic arch and the carotid sinus, with the central nervous system (CNS) using these measurements to provide an appropriate control signal to the BP 'actuators' i.e. the PR and heart, via sympathetic and parasympathetic pathways. In our analysis, we assume that a notional MAP set point is present in the CNS [22], which may be varied, depending on metabolic needs, etc. We also assume that conduction velocity (dromotropy), contraction (inotropy), and relaxation (lusitropy) have more minor effects than cardiac rate (chronotropy), though they are also mediated through sympathetic and parasympathetic neural control [23].

The complete neural baroreflex model [18] is illustrated in Fig. 1, highlighting the baroreceptors, CNS, heart, peripheral resistance and arterial compliance [24] subsystems. The model is parameterised for a New Zealand white rabbit. Note that, while it is beyond the scope of this paper to provide overall

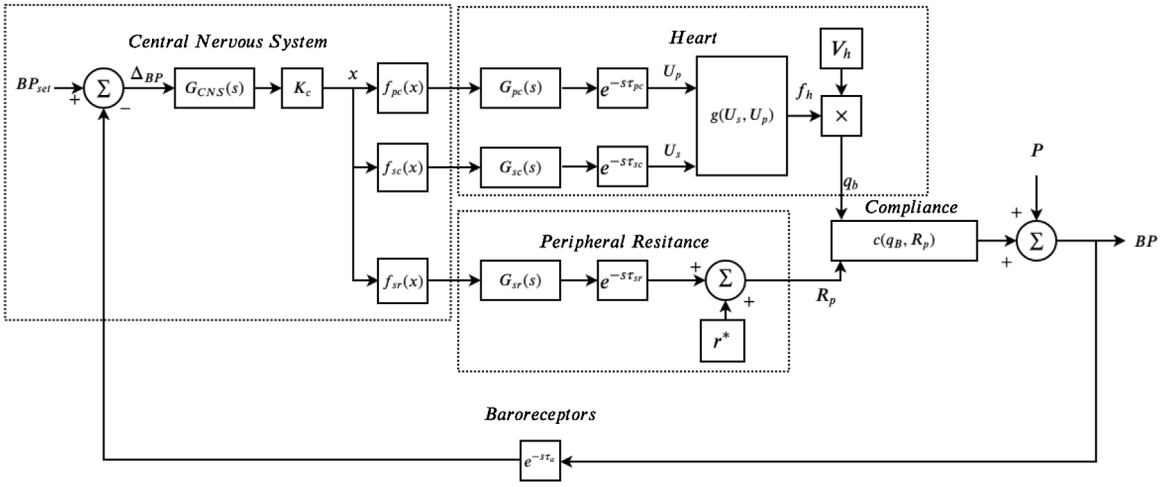

Fig. 1 – The neural baroreflex, containing both peripheral resistance and cardiac branches. P denotes the blood pressure pulsatility component.

Table 1 – Time delays for baroreflex model [25].

τ_{pc}	τ_{sc}	τ_{sr}	τ_a
0.3	0.8	0.85	0.5

model validation with experimental data, each validated model component has been taken from a reliable source.

2.1.1. *Baroreceptors*

The baroreceptors are simply modelled as a nerve conduction delay of τ_a (see Table 1), which also includes the afferent nerve delay [25]. Some researchers [26] have suggested that the baroreceptors may have high-pass frequency characteristics, though it is not entirely clear whether such characteristics are due to the baroreceptors themselves, or the CNS, since typical experiments measure the response in sympathetic nerve activity (SNA) to baroreceptor activation. In any event, the CNS block in our model contains a lead/lag component, articulating both high-pass and low-pass characteristics.

2.1.2. *CNS*

As discussed in Section 2.1.1, the CNS contains a lead/lag component $G_{CNS}(s)$ [18], shown in Eq. (1), along with a variable gain K_c. K_c may vary, depending on physiological condition (e.g. stress, haemorrhage, etc.), leading to the onset, or disappearance of LF oscillations in MAP.

$$G_{CNS}(s) = \frac{1.33s + 1}{s + 1} \tag{1}$$

The CNS also contains the activation characteristics, f_{pc}, f_{sc}, and f_{sr} which articulate the nonlinear steady-state response of parasympathetic cardiac (pc), sympathetic cardiac (sc) and sympathetic peripheral resistance (sr) nerve signals, respectively, to deviations in MAP away from the set point, BP_{set}. f_{pc}, f_{sc}, and f_{sr} are all sigmoidal in form (see Fig. 2), each parameterised with a $tan^{-1}(\,)$ function [27,28]:

$$f(x) = h\ \tan^{-1}(\beta(x - x^*)) + y^*, \tag{2}$$

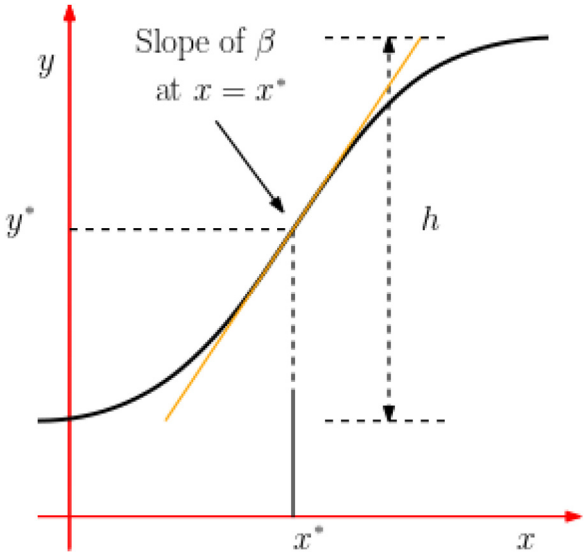

Fig. 2 – Generic $tan^{-1}(\,)$ function related to (2), used to parameterise steady state response of baroreflex to deviations in BP from set point, validated against experimental data in [27].

with parameters as shown in Table 2. Note that, in Table 2, no x^* value is given. Given that we utilise a set point, the base (homeostatic) condition will be that the BP error will be zero (i.e. $x^* = 0$), with the y^* values therefore setting the baseline tone of sympathetic and parasympathetic activity.

2.1.3. *Heart*

The inputs to the heart block are the sympathetic and parasympathetic cardiac signals from the CNS, with the output being blood flow rate. Separate dynamics operate on the sympathetic (G_{sc}) and parasympathetic (G_{pc}) channels [18], via:

Table 2 – Parameters for nonlinear static baroreflex characteristics arctan parameters [18].

Baroreflex Branch	β	h	y^*
Parasympathetic cardiac (pc)	−0.1342	42.5	65.5
Sympathetic cardiac (sc)	0.035	30	42.5
Sympathetic resistance (sr)	0.04	29	185

$$G_{pc}(s) = k_{pc}\frac{1}{1.22s+1}, \tag{3}$$

$$G_{sc}(s) = k_{sc}\frac{1}{1.29s^2+1.29s+1}, \tag{4}$$

where $k_{pc} = 0.148$ and $k_{sc} = 0.181$, while there are also nerve conduction delays of τ_{sc} and τ_{pc} in the sympathetic and parasympathetic channels, respectively (see Table 1). The heart rate has been determined as a nonlinear function of both sympathetic and parasympathetic signals [29,30] from data recorded by Kawada et al. [31] and has been linearised [18] to the following affine function:

$$g(U_p, U_s) = f_h = k_p U_p + k_s U_s + f_o \tag{5}$$

where $k_s = 0.88$, $k_p = -1.2$ [18], and $f_o = 220$ [32] denotes the base heart rate, with value $f_h = 215$ beats/min for a rabbit. Finally, blood flow, q_b, is determined from

$$q_b = f_h V_h \tag{6}$$

where V_h is the heart stroke volume, given as 0.51 cc per kg of body weight, m_r [33], where $m_r = 2.9$ kg [34].

2.1.4. *Peripheral resistance*

The modelled peripheral resistance subsystem focuses exclusively on the neural control of PR, above a base resistance of r^* (taken as $r^* = 0.16$ mmHg/(ml/min) [35]). Hormonal, metabolic, myogenic and paracrinal effects are ignored, given the short timescale of PR effectors considered in this study, and a single branch is used to represent the aggregated effects of innervated resistance in the kidney, muscles, gut, and skin. A sympathetic nerve conduction delay of τ_{sr} (see Table 1) is included in the PR branch, as well as a dynamic block, $G_{sr}(s)$ [34] relating the response in PR to SNA:

$$G_{sr}(s) = k_r\frac{11s^2+6.64s+1}{4.27s^4+21s^3+36s^2+22s+1} \tag{7}$$

where $k_r = 0.0005$.

2.1.5. *Arterial compliance*

Arterial compliance is modelled using a first-order Windkessel model [24] containing resistive (R_p denoting total PR) and capacitive effects, as shown in Fig. 3, and effectively dampening the pulsatile effects of blood flow, due to its low-pass frequency characteristics. A value of $C = 0.000171$ $g^{-1}\,cm^4\,s^2$ [24] was employed.

Considering that R_p is a variable, but appears as a parameter of the Windkessel model, it is potentially problematic from an analytical viewpoint, so an approximation will be employed in Section 2.2.1.

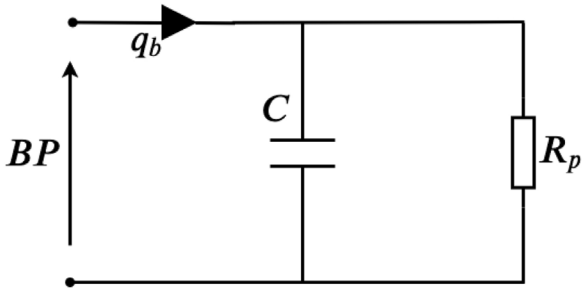

Fig. 3 – 2-element Windkessel model.

2.2. *Model simplification*

One of the main aims of this study is to develop a set of analytical conditions for LF oscillations in the baroreflex. To this end, it is important to have a compact and system-oriented description of the system, and one which, ideally, places the system firmly within the framework of linear time-invariant (LTI) analysis. This, inter alia, requires that the external pulsatile signal be absorbed into a system-type description, and that an effective linearised, but amplitude dependent (describing function), approximation be employed for representation of the nonlinear characteristics f_{pc}, f_{sc}, and f_{sr}. Furthermore, the parametric variation in the Windkessel model is also simplified, to aid analysis.

2.2.1. *Arterial compliance*

A significant difficulty with the arterial compliance model, from an analysis perspective, is that the subsystem currently belongs to the class of linear parameter-varying (LPV) systems. In particular, the relationship between q_b and BP is:

$$\frac{BP(s)}{q_b(s)} = G_c(s) = \frac{R_p(t)}{1+R_p(t)Cs} \tag{8}$$

where $R_p(t)$ is a time varying parameter of the system. It is possible to retain the essence of the effect of a varying R_p by using the true value of R_p in the numerator of (8), while using a constant (mean) value, $\overline{R_p}$ in the denominator of (8):

$$\frac{BP'(s)}{p_b(s)} = G_c'(s) = \frac{1}{1+\overline{R_p(t)}Cs}, \tag{9}$$

where p_b is the MAP signal derived from the classic Ohm's law relationship, excluding compliance, as:

$$p_b = q_b R_p, \tag{10}$$

as demonstrated in Fig. 4. This is justified by the fact that the main effect is a *gain* change, due to the numerator instance of R_p (note that the dc gain of (8) is $R_p(t)$), while a variation in the dynamic response around the mean value of R_p in the denominator ($\overline{R_p}$) will be minimal. Though the system on the right-hand side of Fig. 4 is still parameter varying, it is significantly easier to analyse. A steady-state analysis yields:

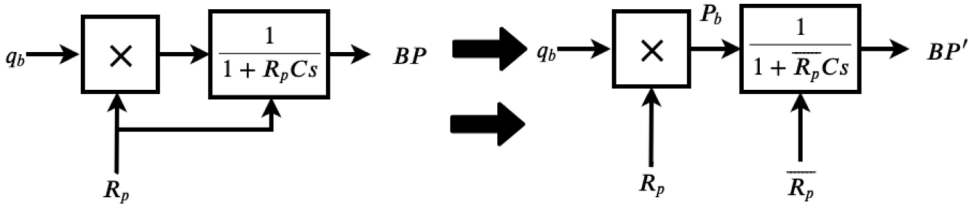

Fig. 4 – Compliance approximation for the analytical solution.

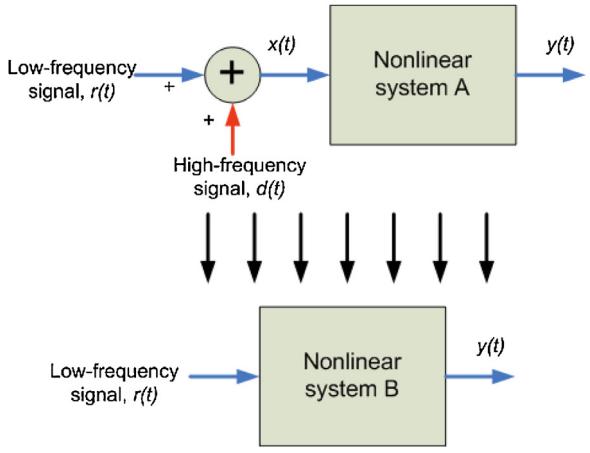

Fig. 5 – Equivalent nonlinearity concept.

$$\overline{R_p} = r^* + G_{sr}(0)y^*_{sr} \tag{11}$$

2.2.2. *Pulsatility effects*

The pulsatile component, P, of the BP signal is absorbed into the static nonlinear characteristics, f_{pc}, f_{sc}, and f_{sr} to produce *equivalent nonlinearities* f^e_{pc}, f^e_{sc}, and f^e_{sr}. This provides a significant simplification by observing the frequency separation between the variations in MAP (which include LF oscillations) and pulsatility. In the 'equivalent nonlinearity' (EQNL) procedure, a system with an input x(t), containing a relatively LF input r(t) and a high frequency 'dither' signal d(t), can be represented as a modified nonlinear system [36], as shown in Fig. 5. Here, the procedure for the determination of an EQNL is outlined, developing a new nonlinearity (Nonlinear system B ($f^e(x)$)), subject only to a LF signal r(t), from an original nonlinear system A ($f(x)$) which is subject to LF (r(t)) and HF (d(t)) signals. For further details, see [36] and [19]. Since the EQNL is specific to the nature of the dither signal d(t) employed, a typical pulsatile BP signal from a rabbit is employed [37], as shown in Fig. 6.

With an original nonlinear system $y = f(x)$, where $x = r(t) + d(t)$, gives:

$$y = f(r(t) + d(t)) \tag{12}$$

The output of the EQNL corresponding to the nonlinear system is:

$$\overline{y} = \int_{-\infty}^{\infty} f(r(t) + q)\, p(q)\, dq \tag{13}$$

where $p(q)dq$ is the probability that, for any time t, the dither signal d(t) lies in the range q to $q + dq$, and $d(q)$ is the probability density function for the dither signal. The probability density function for the dither signal is:

$$p(q) = -\frac{dF(p)}{dp} = \frac{1}{2A} \tag{14}$$

The parameters for the dither signal were obtained from a piecewise linear approximation of the clinical measurement of BP in the abdominal aorta of a rabbit [37]. One cycle of the data

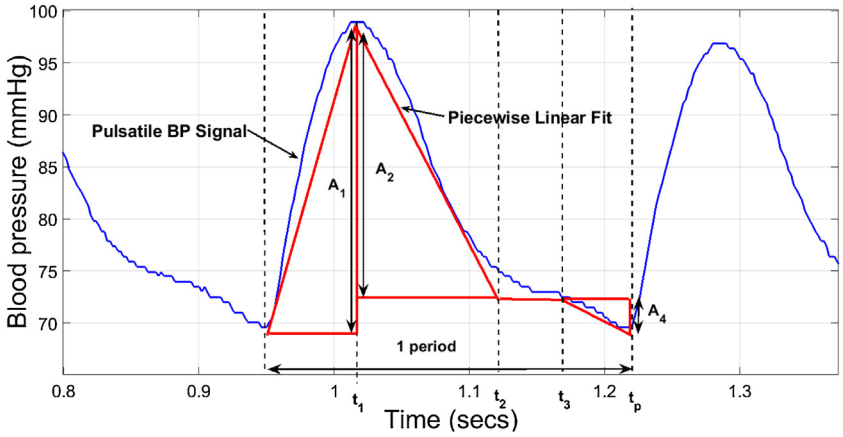

Fig. 6 – Piecewise linear approximation of one BP cycle.

was divided into 4 segments, three triangles and one flat line, with the fit, as shown in Fig. 6, determined manually. The specific parameters for each segment can be found in Table 3. It is found that the EQNL is not especially sensitive to the finer details of the dither signal, with the amplitude extremes and proportion of positive/negative transition the dominant influences.

Segments 1, 2 and 4 are represented by triangles with varying heights, A, and their respective EQNL outputs can be obtained by inserting the appropriate A into Eq. (15):

$$\overline{y_{i=1,2,4}} = \int_{b-A_i}^{b+A_i} \frac{1}{2A_i}[h\tan^{-1}(\beta(r+q)) + y^*]dq \tag{15}$$

$$\begin{aligned}\overline{y_{i=1,2,4}} \quad = \quad & \frac{h}{2A_i}((r+q)\tan^{-1}(\beta(r+q))) \\ & -\frac{h}{4A_i\beta}\ln|\beta^2(r+q)^2+1| + y^*(r+q))|_{b-A_i}^{b+A_i}\end{aligned} \tag{16}$$

Segment 3 is approximated by a flat line, resulting in a constant probability function and giving an EQNL output of:

$$\overline{y_3} = h\ \tan^{-1}(\beta(r+q)) + y^* \tag{17}$$

The total EQNL output is the sum of all four segment components, weighted by factors α_i, corresponding to the relative portions of the total period $t_p - t_o$, from Fig. 6:

$$\overline{y} = \alpha_1\overline{y_1} + \alpha_2\overline{y_2} + \alpha_3\overline{y_3} + \alpha_4\overline{y_4} \tag{18}$$

where $\alpha_1 = 0.252$, $\alpha_2 = 0.385$, $\alpha_3 = 0.167$, $\alpha_4 = 0.196$. Note that $\Sigma\alpha_i = 1$. In order to get the $f \to f^e$ for each of f_{pc}, f_{sc}, and f_{sr}, Eq. (18) is used in conjunction with (16) and (17), with the appropriate β and y^* values for $\overline{y_1}$, $\overline{y_2}$, $\overline{y_3}$, and $\overline{y_4}$ taken from Table 2, as appropriate.

Note that, since the EQNL depends only on the relative areas of the piecewise approximations to the pulsatile signal segments, and the proportions of the period occupied by those segments, but *not* on the period of the dither signal itself (so long as $d(t)$ is significantly HF, relative to $r(t)$, for example by an order of magnitude, which would be a typical ratio between heart-rate and LF oscillation, across different species), a fixed frequency for $d(t)$ (effectively the heart rate) can be used in subsequent analysis and simulation.

2.2.3. *Describing function approximation*

The static nonlinear characteristics, f_{pc}, f_{sc}, and f_{sr}, are represented by their *describing functions*, simplifying the analytical manipulation of the functions f_{pc}, f_{sc}, and f_{sr}. The describing function (DF) approximation essentially assumes a sinusoidal input to a nonlinearity (useful for the analysis of LF oscillations) and calculates the effective 'gain' of the system (which is dependent on amplitude of the input) with respect to the fundamental component of the output [38]. For the $tan^{-1}()$ function of Eq. (2) and Fig. 2, the DF has been calculated [27] as:

$$\mathrm{DF}(X) = \frac{2h}{\beta X^2}\left(\sqrt{1+\beta^2X^2} - 1\right) \tag{19}$$

where the input to the nonlinearity is $x(t) = X\ sin(\omega t)$. The expression in (19) may be further simplified [27] for asymptotic values of X to:

$$\mathrm{DF}(X) \to \frac{2\ h}{X}, \quad X \to \infty \tag{20}$$

for large X and,

$$\mathrm{DF}(X) = h\beta(1-\beta^2X^2), \quad X \to 0. \tag{21}$$

for small X. The use of the DF in this application is justified, since the major assumption that the DF relies on, i.e. that output harmonics are significantly attenuated, is satisfied through G_{pc}, G_{sc} and G_{sr} all having low-pass frequency response characteristics. Furthermore, we are primarily interested in the propagation of LF (fundamental) oscillations, rather than the existence of harmonic components. In any case, the dominance of the fundamental will be demonstrated in Section 3.1.2.

2.3. *LF oscillations*

Using the model of Section 2.1, LF oscillations can be analysed in two ways. The first, and most direct, approach is to simulate the model of Fig. 1 and examine for conditions under which oscillations in *BP* occur. While such simulation studies are useful, they provide little indication of the bigger picture, outside the set of specific tests performed. It would therefore be beneficial if an alternative analytical route could be pursued, employing the simplifications of Section 2.2.

In [2], it was possible to employ a DF approximation in combination with classical (linear) Nyquist stability analysis to determine conditions under which LF oscillations would occur. In that analysis, the gain of the CNS was seen to be instrumental in the modulation of LF oscillations, as will be shown in the current case. However, for the model of Fig. 1, such an approach is not possible, given the multiple branches and diverse dynamics in each path. Rather, an approach, inspired by [18], is employed, where a notional LF (sinusoidal) oscillatory signal is injected at $x(t)$, and propagated around the baroreflex, to determine a set of conditions under which the original signal might arrive back at $x'(t)$ i.e. the conditions for sustained oscillations, as shown in Fig. 7.

If sustained oscillations occur, assuming the fundamental component of $x'(t)$ to be $x''(t) = A''\sin(\omega''t + \phi'') + \overline{X''}$, then the following must hold:

$$\omega'' = \omega', \tag{22}$$

$$A'' = A', \tag{23}$$

$$\phi'' = 0, \tag{24}$$

$$\overline{X''} = 0, \tag{25}$$

Table 3 – Segmentation of clinical data.

Parameter	$t_o - t_1$	$t_1 - t_2$	$t_2 - t_3$	$t_3 - t_p$
A (height)	29.18	26.02	0	3.37
τ (length)	0.068	0.104	0.0452	0.053

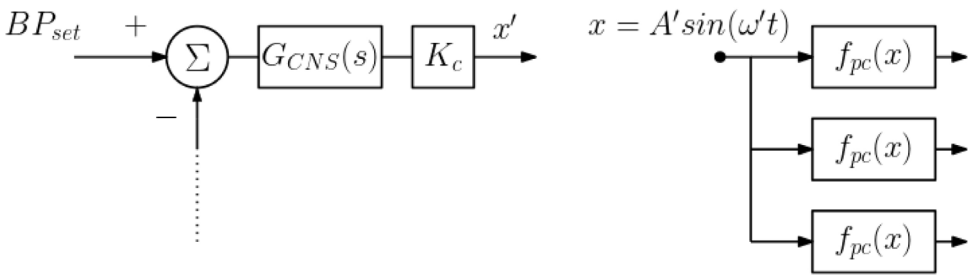

Fig. 7 – Break in loop to determine conditions for sustained oscillation.

corresponding to conditions on frequency, amplitude, phase and offset, respectively. We assume that x(t) has no dc component, since the system of Fig. 1 is assumed to be in homeostasis (see more on this in Section 3).

Using the configuration in Fig. 7, the signal x(t) first passes through the three nonlinearities, f_{pc}, f_{sc} and f_{sr}, resulting in the DF outputs:

$$z_{pc} = DF_{pc}A'\sin(\omega' t) + y^*_{pc} \tag{26}$$

with

$$DF_{pc} = \frac{2h_{pc}}{\beta_{pc}A'^2}\left(\sqrt{1+\beta_{pc}{}^2A'^2}-1\right), \tag{27}$$

$$z_{sc} = DF_{sc}A'\sin(\omega' t) + y^*_{sc} \tag{28}$$

with

$$DF_{sc} = \frac{2h_{sc}}{\beta_{sc}A'^2}\left(\sqrt{1+\beta_{sc}{}^2A'^2}-1\right), \tag{29}$$

and

$$z_{sr} = DF_{sr}A'\sin(\omega' t) + y^*_{sr} \tag{30}$$

with

$$DF_{sr} = \frac{2h_{sr}}{\beta_{sr}A'^2}\left(\sqrt{1+\beta_{sr}{}^2A'^2}-1\right), \tag{31}$$

The heart output flowrate, f'_h, is now:

$$f'_h = N_{pc}\sin(\omega' t + \phi_{pc}) + N_{sc}\sin(\omega' t + \phi_{sc}) + \overline{f_h} \tag{32}$$

where,

$$N_{pc} = k_p k_{pc}|G_{pc}(\omega')|DF_{pc}A', \tag{33}$$

$$\phi_{pc} = \angle G_{pc}(\omega') - \omega'\tau_{pc}, \tag{34}$$

$$N_{sc} = k_s k_{sc}|G_{sc}(\omega')|DF_{sc}A', \tag{35}$$

$$\phi_{sc} = \angle G_{sc}(\omega') - \omega'\tau_{sc}, \tag{36}$$

$$\overline{f_h} = k_p k_{pc} y^*_{pc} + k_s k_{sc} y^*_{sc} + f_o. \tag{37}$$

or

$$N_c\sin(\omega' t + \phi_c) + f_h \tag{38}$$

where

$$\phi_c = \tan^{-1}\frac{N_{pc}\sin(\phi_{pc}) + N_{sc}\sin(\phi_{sc})}{N_{pc}\cos(\phi_{pc}) + N_{sc}\cos(\phi_{sc})}, \tag{39}$$

$$N_c = \sqrt{i^2 + j^2}, \tag{40}$$

with

$$i = N_{pc}\cos(\phi_{pc}) + N_{sc}\cos(\phi_{sc}), \tag{41}$$

$$j = N_{pc}\sin(\phi_{pc}) + N_{sc}\sin(\phi_{sc}). \tag{42}$$

From (6),

$$q'_b = V_h N_c \sin(\omega' t + \phi_c) + \overline{q'_b} \tag{43}$$

where

$$\overline{q'_b} = V_h \overline{f_h}, \tag{44}$$

Now propagating $z_{sr}(t)$ through the peripheral resistance branch, get

$$R'_p = N_{sr}\sin(wt + \phi_{sr}) + \overline{r} \tag{45}$$

where,

$$N_{sr} = k_r|G_{sr}(\omega')|DF_{sr}A' \tag{46}$$

$$\phi_s r = \angle G_{sr}(\omega') - \omega'\tau_{sr} \tag{47}$$

$$\overline{r} = k_r y^*_{sr} + r^* \tag{48}$$

The cardiac (43) and resistance (45) branches are combined via the simplified arterial compliance model as shown in Fig. 4:

$$BP' = |G_c(\omega')|N_p\sin(\omega' t + \phi_p) + k(\omega') + \angle G_c(\omega') + \overline{r}\,\overline{q'_b} \tag{49}$$

where

$$\phi_c = \tan^{-1}\frac{N^*_c\sin(\phi_c) + N^*_{sr}\sin(\phi_{sr})}{N^*_c\cos(\phi_c) + N^*_{sr}\cos(\phi_{sr})} \tag{50}$$

$$N^*_c = \overline{r}V_h N_c \tag{51}$$

$$N^*_{sr} = \overline{q'_b}N_{sr} \tag{52}$$

$$k(\omega) = \frac{V_h N_c N_{sr}}{2}\cos(\phi_c - \phi_{sr}) \tag{53}$$

$$N_p = \sqrt{m^2 + n^2} \tag{54}$$

with

$$m = N_c^* \cos(\phi_c) + N_{sr}^* \cos(\phi_{sr}) \tag{55}$$

$$n = N_c^* \sin(\phi_c) + N_{sr}^* \sin(\phi_{sr}) \tag{56}$$

Note that, in (53), the amplitude of the harmonics of ω' are assumed to be negligible compared with the fundamental, so just the fundamental component is retained. This is justified, as in Section 2.2.3, by the fact that the dynamics of G_{pc}, G_{sc}, and G_{sr} are low-pass and therefore attenuate relatively high frequency harmonics, with further validation in Section 3.1.2.

The BP' signal is now fed back through the baroreceptor delay to the CNS dynamics:

$$\begin{aligned} x''(t) \;=\; & K_c|G_{CNS}(\omega')|\{PB_{set} - \bar{r}\,\overline{q_b'} \\ & -k(\omega') - N_p \sin(\omega' t + \phi_p \\ & -\omega'(\tau_a) + \angle G_{CNS}(\omega') + \pi)\} \end{aligned} \tag{57}$$

Since we have assumed, in (53), that the harmonics of BP' are negligible, x'' in (57) clearly contains only the fundamental component of ω' and the condition of (22) becomes redundant. The amplitude condition of (23), in residual form, from (57), becomes:

$$K_c|G_{CNS}(\omega')||G_c(\omega')|(\omega')K_P - A' = 0 \tag{58}$$

while the phase and offset conditions of (24) and (25) become, respectively:

$$\phi_p - \omega'(\tau_a) + \angle G_{CNS}(\omega') + \angle G_c(\omega') + \pi = 0 \tag{59}$$

and

$$K_c|G_{CNS}(\omega')|\{PB_{set} - \bar{r}\,\overline{q_b'} - k(\omega')\} = 0. \tag{60}$$

Eqs. (58)–(60) describe the set of conditions of sustained oscillations with a fundamental frequency ω'.

2.3.1. Solution to equations

From Eqs. (58)–(60), we can identify the cost function to minimise as:

$$J = \sum_{i=1}^{3} \gamma_i r_i^2 \tag{61}$$

where

$$\begin{aligned} r_1 &= K_c|G_{CNS}(\omega')||G_c(\omega')|(\omega')K_P - A', \\ r_2 &= \phi_p - \omega'(\tau_a) + \angle G_{CNS}(\omega') + \angle G_c(\omega') + \pi, \\ r_3 &= K_c|G_{CNS}(\omega')|\{PB_{set} - \bar{r}\,\overline{q_b'} - k(\omega')\}. \end{aligned}$$

where the weighting factors γ_i reflect the relative magnitude units of the r_i.

The Levenberg-Marquardt algorithm [39] is used to solve the non-linear least squares problem represented by minimising (61). In order to investigate the sensitivity of the solution to the optimisation algorithm used, trust-region [40] and simplex [41] algorithms were also tested, giving consistent results.

2.4. Preliminary calculations

2.4.1. Homeostatic analysis

In order to prove that the system, from a static balance point of view (homeostasis), is consistent, a steady-state analysis is performed. Under such conditions, the BP error Δ_{BP} should be zero and all dynamic blocks reduce to their dc gain, as shown in Fig. 8. Also, the arterial compliance subsystem reverts to the 'Ohm's law' relationship of (10). Since $\Delta_{BP} = 0$, the outputs of f_{pc}, f_{sc}, and f_{sr} are y_{pc}^*, y_{sc}^*, and y_{sr}^*, respectively, as given in Table 2. Under these conditions, BP is 80 mmHg, which is consistent with the condition $\Delta BP = BP_{set} - BP$ specified in Fig. 1, confirming homeostasis. While the specific value of $Bp_{set} = 80$ mmHg is not crucial in confirming homeostasis, it has been chosen as typical of a normotensive rabbit (see, for example, the experimental data in Fig. 6).

2.4.2. EQNL calculations

Following the procedure in Section 2.2.2, the *equivalent nonlinearities* f_{pc}^e, f_{sc}^e, and f_{sr}^e are now determined for the nonlinear characteristics f_{pc}, f_{sc}, and f_{sr}, shown in Fig. 9.

Note that a $tan^{-1}(\,)$ fit has been generated to the EQNL in each case, so that a specific change in the linearised 'gain' at (x^*, y^*), due to the presence of pulsatility, may be calculated for each case. The results are shown in Table 4. It may be noted, from Fig. 9 that, while the fit of the $tan^{-1}(\,)$ function to the EQNL is generally good in the region of the function origin, it is less good at the extremities. This is deliberate, in trading off error in central values for extreme values, within the limits of approximation of the fitted $tan^{-1}(\,)$ functions. Specifically, the EQNL is precisely matched at the origin, so that a representative β value can be determined for the EQNL. If desired, a more precise parametric approximation can be determined using a combination of parametric functions, including an $tan^{-1}(\,)$ and a saturation characteristic [19].

2.4.3. Determining a value for K_c

The value for K_c is not well defined, since any experimental evaluation would require that all nerve fibres at the outputs of f_{pc}, f_{sc}, and f_{sr} are fully recruited, which is impossible to achieve in experimental practice. However, K_c can be estimated by recognising that K_c is primarily responsible for mediating LF oscillations [2], and it therefore seems likely that the brain modulates K_c in response to different adverse physiological conditions e.g. hypoxia [42], haemorrhage [43], etc. In particular, given that LF oscillations are instigated/accentuated during adverse physiological conditions, one possibility is to establish a value of K_c in the 'normal' physiological state (including pulsatility) which is just below that required to initiate LF oscillations. This value is set at $K_c^{nom} = 7$ for the (normal) pulsatile case, where a 10% increase results in the onset of LF oscillations. Therefore, a reasonably substantial effective increase in overall baroreflex gain (due to a lack of pulsatility or otherwise) is required to instigate LF oscillations.

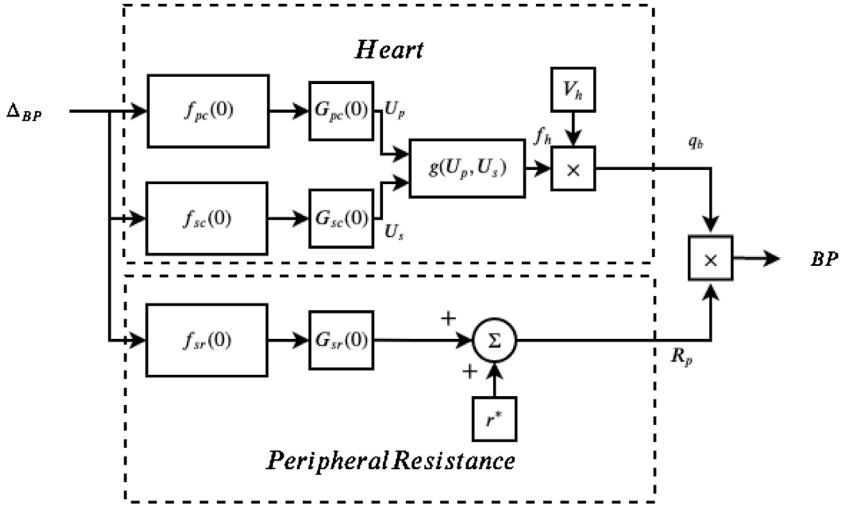

Fig. 8 – Homeostatic analysis of the neural baroreflex.

2.5. *Sensitivity calculations*

Given that, in the model of Fig. 1, there are multiple paths via which the neural control of BP is effected, and BP oscillations may propagate, a reasonable question might arise as to the predominance of any of these branches. To examine the relative strength/gain of each of the branches of the model in Fig. 1, we perform a simple sensitivity study, which examines the raw (dc) gain from Δ_{BP} to BP, from the simplified model of Fig. 8. While a dc analysis does not include the dynamic effects of G_{pc}, G_{sc} and G_{sr}, their effects will be relatively consistent between paths, and their low-pass cutoff frequency is relatively high, compared to the LF oscillation's frequency of 0.33 Hz, as are the arterial compliance dynamics.

From Fig. 8, the following may be easily calculated:

$$S_{sr}^{BP} = \frac{dBP}{d\Delta_{BP}}\Big|_{\substack{f_{pc}=y_{pc}^* \\ f_{sc}=y_{sc}^*}} = \overline{q_b}\, k_{sr}\beta_{sr} \tag{62}$$

which articulates the sensitivity of BP to Δ_{BP} along the peripheral resistance path, and

Table 4 – Modification of β values due to pulsatility.

Arctan function	β_{pc}	β_{sc}	β_{sr}
Original Arctan (Case 1 &2)	−0.1342	0.035	0.04
EQNL Arctan (Case 3)	−0.1342*0.55	0.035*0.875	0.04*0.82

$$S_c^{BP}\frac{dBP}{d\Delta_{BP}}\Big|_{f_{sr}=y_{sr}^*} = \overline{R_p}V_h(k_p k_{pc}\beta_{pc} + k_s k_{sc}\beta_{sc}) \tag{63}$$

which articulates the sensitivity of BP to Δ_{BP} along the complete cardiac path (pc & sc), where $\overline{R_p}$ is given from Eq. (11) and

$$\overline{q_b} = V_h(k_p k_{pc} y_{pc}^* + k_s k_{sc} y_{sc}^* + f_o) \tag{64}$$

The individual sensitivities along the parasympathetic and sympathetic cardiac branches can also be evaluated, respectively, as:

$$S_{pc}^{BP} = \frac{dBP}{d\Delta_{BP}}\Big|_{\substack{f_{sr}=y_{sr}^* \\ f_{sc}=y_{sc}^*}} = \overline{R_p}V_h k_p k_{pc}\beta_{pc} \tag{65}$$

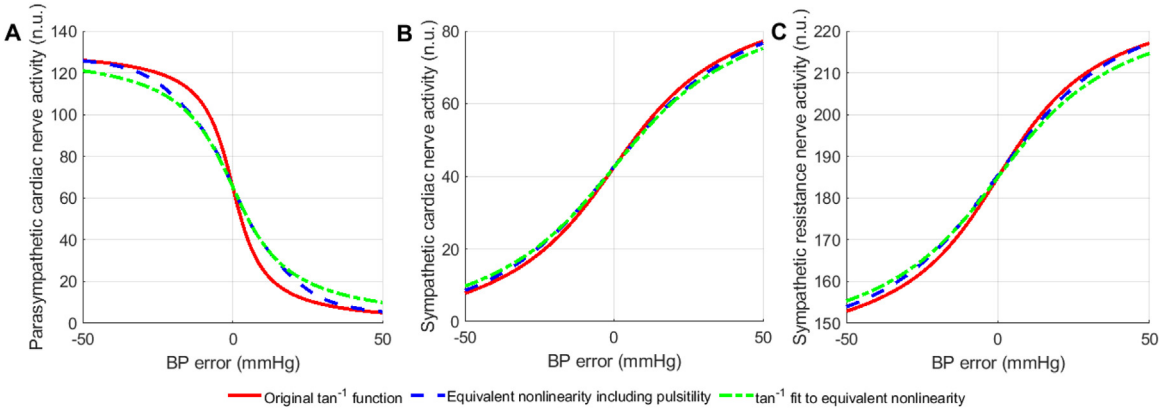

Fig. 9 – Changes in the activation parameters, β_{pc}, β_{sc}, and β_{sr}, with the inclusion of pulsatility.

and

$$S_{sc}^{BP} = \frac{dBP}{d\Delta_{BP}}\Big|_{\substack{f_{sr}=y_{sr}^{*} \\ f_{pc}=y_{pc}^{*}}} = \overline{R_p} V_h k_s k_{sc} \beta_{sc} \tag{66}$$

3. Results

3.1. LF oscillations

LF oscillations are now initiated by an increase in K_c by 25% over the nominal value calculated in Section 2.4.3, consistent with the data in [27] showing a 25% increase in β in the change from normoxia to hypoxia (10% O_2 + 3%CO_2). In our simulation, this will be effected by an increase in K_c from its nominal value of $K_c = 7$ to $K_c' = 1.25K_c^{nom} = 8.75$. This is confirmed by both the analytical solution from Eqs. (58)–(60), and computer simulation of the model in Fig. 1, using the Matlab/Simulink platform.

3.1.1. Analytical solution

For a value of K_c', the performance surface for (61) is shown in Fig. 10, showing a broadly convex surface. The algorithm found a local minimum at $\omega = 0.3187$ Hz and $A' = 16.4504$, for an initial value range of $0.25\text{ Hz} < \omega < 0.45\text{ Hz}$ and $10 < A < 50$, which also defines the maximum domain of attraction within which this solution can be found. For a uniform residual weighting ($\gamma_i = 1$, $1 \le i \le 3$), a residual vector of $[r_1\ r_2\ r_3] = [-1.0656 - 0.1244\ 0.0439]$ is obtained.

The most useful solution parameters from the minimisation of (61) are ω' and A', which give the frequency and amplitude of the LF oscillations, respectively. The examination of A' may be used as binary indication of oscillations, where a value of $A' = 0$ indicates no oscillations. Fig. 11 shows the change in oscillation amplitude (A') with variation in K_c. Note the expected threshold at $K_c = 7.7$ for the normal (pulsatile) case.

3.1.2. Simulation results

Fig. 12 shows the relative magnitude of the LF oscillation's fundamental, and confirms that harmonic amplitudes are small (<10%) compared to the fundamental amplitude. This confirms the validity of ignoring the harmonics of the fundamental frequency ω' in the analysis of Section 2.3. However, while a fundamental-based analysis for the solution of LF oscillations may be appropriate, the presence of harmonics means that the LF oscillations are not perfectly sinusoidal, though this not obviously apparent from the time domain plot of Fig. 13.

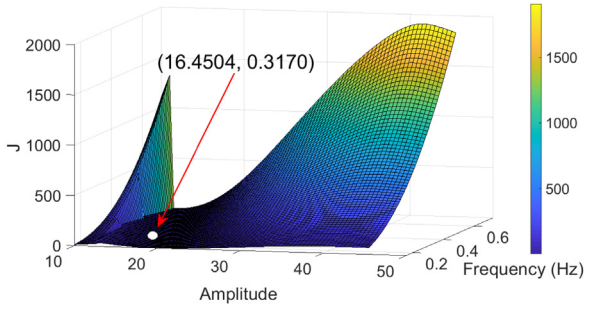

Fig. 10 – Performance surface for $J = \sum_{i=1}^{3} \gamma_i r_i^2$, showing optimal solution for (A', ω').

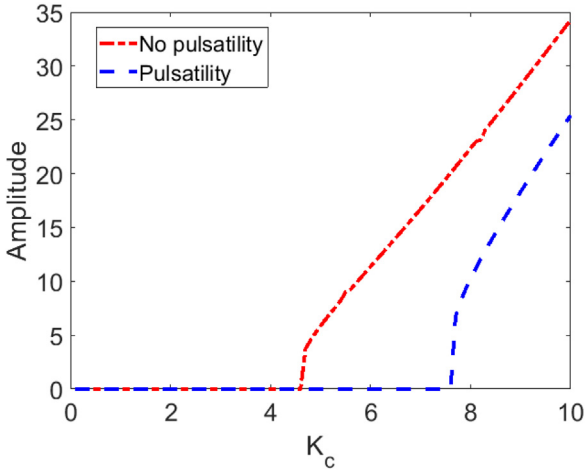

Fig. 11 – Investigating the threshold of K_c.

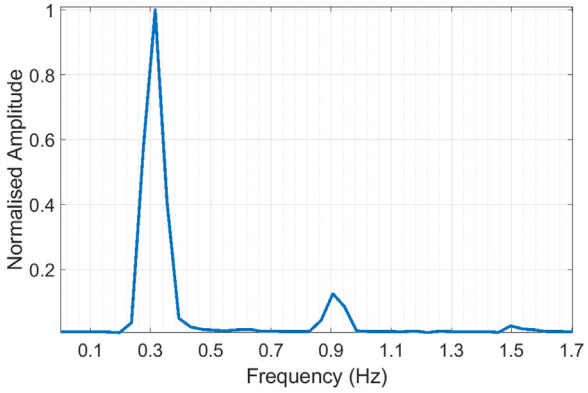

Fig. 12 – Harmonics present in BP signal during LF oscillations.

While simulation results confirm that no LF oscillations take place for the nominal value of $K_c^{nom} = 7$, Fig. 13 also confirms the situation for $K_c = 7(1 + 0.25) = 8.75$, where a LF BP oscillation of 1.34 mmHg occurs, consistent with the analytical solution of Section 3.1.1. The specific comparative results for analytical/simulation cases are shown in Table 5, showing good agreement (deviation is 5.6% for the analytical solution and 2.3% for the simulation) with the experimental LF BP oscillation frequency of 0.3 Hz reported in [21].

3.2. Removing pulsatility

Under certain medical interventions, blood pulsatility may be reduced or eliminated, for example by insertion of an artificial (turbine-type) heart, or the inclusion of a LVAD. The effect of pulsatility on the neural baroreflex can be examined both via manipulation of the baroreflex functions f_{pc}, f_{sc}, and f_{sr}, or by inclusion/exclusion of the pulsatility component P in the simulation.

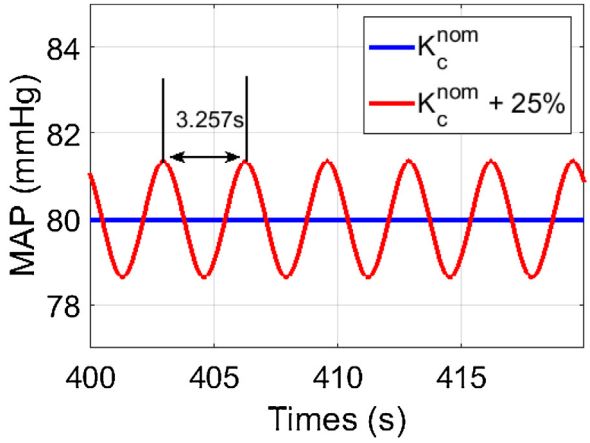

Fig. 13 – LF oscillations in BP for the normal (pulsatile) case, for nominal and increased K_c values. The LF oscillations is measured at a period of 3.257 s, corresponding to a frequency of 0.307 Hz.

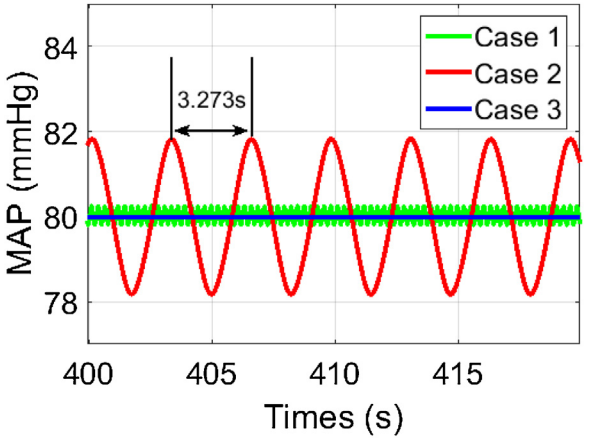

Fig. 14 – Simulation results for the pulsatile (Cases 1 and 3) and non-pulsatile cases (Case 2), where pulsatility is represented both by EQNL values or the inclusion of a physical pulsatility signal P. Note that $K_c = K_c^{nom}$. The three cases illustrated are documented in Table 6.

Some initial indication can be had from examination of Fig. 9. In particular, with reference to Table 4, it is clear that the *addition* of pulsatility causes a significant *reduction* in overall baroreflex gain, demonstrated by the decrease in the β_{xx} from their 'original' values to their EQNL values, with a gain reduction of up to 55% (for β_{pc}). The change in baroreflex gain, resulting from an absence of pulsatility, is confirmed by the simulation, where Fig. 14 shows the appearance of LF oscillations, following the removal of pulsatility (Case 2), consistent with experimental evidence [17]. Pulsatility can therefore be represented, for simulation purposes, either by including a pulsatile component P in the BP signal, as shown in Fig. 1 (Case 1), or by omitting P but using the EQNL values for the β_{xx} (Case 3). Table 6 shows 3 cases examined, including both pulsatility, using both an explicit P component or the EQNL values for the β_{xx}, and a non-pulsatile scenario, where original β_{xx} values are used and P is omitted. Fig. 11 shows the variation in oscillation amplitude (A') with variations in K_c for the non-pulsatile case (red trace). Note the significant reduction in the threshold value of K_c. In Fig. 14, the trace for Case 1 (see Table 6) contains the pulsatile (green line) BP which is not completely dampened by arterial compliance, but confirms consistence with the trace for Case 3, i.e. the absence of LF oscillations.

3.3. *Predominance of resistance or cardiac branches*

Following the sensitivity functions developed in Section 2.5, Table 7 shows the enumerated values for the sensitivity functions in (62)–(66). The sensitivity values suggest a predominance of the cardiac branch over the resistance branch, while the parasympathetic cardiac is favoured over the sympathetic cardiac.

Simulation studies were undertaken to examine the relative importance of various branches in mediating LF oscillations and Table 7 also shows the achieved oscillation amplitude (OA) in BP and the associated oscillation frequency, for removal of various branches (for example, in the pc column, only the pc branch is active). The simulation results are quite revealing. For a value of $K_c = K_c'$ (with pulsatility included), no single branch is capable of supporting LF

Table 5 – Comparative LF oscillation amplitude for analytical and simulation results.

Case	A'	BP osc. ampl. (mmHg)	Osc. freq. (Hz)
Analytical soln.	16.4504	~ 1.38	0.317
Simulation	15.1	~ 1.34	0.307

Table 6 – Test conditions.

Case	Baroreflex function parameters	Pulse signal P present
1	f_{xx}	Yes
2	f_{xx}	No
3	f_{xx}^e	No

Table 7 – Sensitivity values for propagation through various cardiac and resistance branches, using a dc gain approximation, along with LF oscillations BP amplitudes (OA, in mmHg) for corresponding branches from simulation.

Branch	K_c	sr	c	pc	sc
Sensitivity fn.	–	S_{sr}^{BP}	S_c^{BP}	S_{pc}^{BP}	S_{sc}^{BP}
Sensitivity (x10^{-4})	–	53	67	50	17
BP OA	K_c'	0	0	0	0
BP OA	$2K_c'$	0.86	0.79	0.99	0
Frequency		0.256	0.384	0.400	0
BP OA	$3K_c'$	1.96	1.10	1.32	0.19
Frequency		0.256	0.384	0.400	0.169

oscillations. As K_c is increased (to $2K_c'$, and subsequently to $3K_c'$), individual branches become capable of sustaining LF oscillations but, crucially, none of the achieved LF oscillations frequency values correspond with experimental evidence [21]. This is primarily due to the variety of conduction and phase delays in each individual branch, while the full model contains a mixture of these dynamical components that appears to correctly articulate the oscillations observed experimentally. Overall, there is a strong suggestion that both cardiac and resistance branches are crucial in the support of LF BP oscillations. Interestingly, Liu et al. [44] conclude that the cardiac branch is relatively unimportant in the dynamic regulation of BP and the mediation of LF oscillations in MAP. However, their results do show an 8 dB (equivalent to a factor of 2.5) drop in gain between 0.1 and 0.3 Hz due to vagotomy and β_1-receptor blockade (effectively inhibiting neural control of cardiac output), which this study has shown to be significant in mediating LF oscillations, given that a 10% increase in baroreflex gain could, potentially, instigate LF oscillations.

4. Discussion

The paper presents a model for the neural baroreflex focused on the components that mediate LF oscillations in BP. A number of analytical tools are employed to render the model amenable to an algebraic solution for LF oscillations conditions, which gives some insight into the role that baroreflex gain plays in mediating LF oscillations. In particular, changes in the 'gain' of the central nervous system are shown to be a key factor, which can result from external stimulus or internal stress (e.g. haemorrhage, hypoxia, etc.). In particular, the use of the 'equivalent nonlinearity', in representing pulsatility, reveals a significant increase in overall baroreflex gain as a result of a *loss of pulsatility*, which may have important implications for patients in receipt of artificial (turbine-based) hearts, or LVADs. Such an increase in baroreflex gain is shown to precipitate an elevation in LF oscillations, which is borne out by experimental evidence [17]. In addition, the increase in experimentally measured LF oscillations following LVAD insertion documented in [7] in R-R is consistent with the analytical results developed in this paper relating to the role of the heart in mediating LF oscillations and an increase in baroreflex gain following a drop in pulsatility. However, it should also be noted that the study of Cooley et al. [7] did not report an increase in LF MAP oscillations, opening the possibility that the steady flow from the autonomous LVAD may have dominated the native cardiac output. While experimental evidence therefore exists which ties pulsatility decreases (LVAD insertion) to increases in baroreflex gain, and LVAD insertion to the increased presence of LF oscillations in R-R interval, the mechanisms by which these are linked has, to date, remained unclear. We hope that the unifying framework in this paper provides a plausible explanation for these experimentally observed phenomena.

Overall, the model, and the analysis contained in the paper, provides a toolbox for the analysis of the interplay between baroreflex gain, LF oscillations and blood pulsatility. One of the important conclusions is that LF oscillations are mediated by a combination of cardiac and peripheral resistance branches, while establishing the key role of baroreflex gain as the mechanism by which LF oscillations are modulated. In turn, the baroreflex gain is seen to be substantially influenced by pulsatility and physiological stress.

Declarations of interest

None declared.

Acknowledgements

The authors are grateful for the fruitful discussions with Dr. Sarah-Jane Guild and Prof. Simon Malpas of the Dept. of Physiology at the University of Auckland Medical School, New Zealand.

REFERENCES

[1] Julien C. The enigma of Mayer waves: facts and models. Cardiovasc Res 2006;70(1):12–21.
[2] Ringwood JV, Malpas SC. Slow oscillations in blood pressure via a nonlinear feedback model. Am J Physiol – Regul Integr Comp Physiol 2001;280(4):R1105–1.
[3] Moazami N, Dembitsky WP, Adamson R, Steffen RJ, Soltesz EG, Starling RC, et al. Does pulsatility matter in the era of continuous-flow blood pumps? J Heart Lung Transplant 2015;4(8):999–1004.
[4] Vašků J, Wotke J, Dobšák P, Baba A, Rejthar A, Kuchtícková Š, et al. Acute and chronic consequences of non-pulsatile blood flow pattern in long-term total artificial heart experiment. Pathophysiology 2007;14(2):87–95.
[5] Timms D. A review of clinical ventricular assist devices. Med Eng Phys 2011;33(9):1041–7.
[6] Slaughter MS, Rogers JG, Milano CA, Russell SD, Conte JV, Feldman D, et al. Advanced heart failure treated with continuous-flow left ventricular assist device. N Engl J Med 2009;361:2241–51.
[7] Cooley RL, Montano N, Cogliati C, Van de Borne P, Richenbacher W, Oren R, et al. Evidence for a central origin of the low-frequency oscillation in rr-interval variability. Circulation 1998;98(6):556–61.
[8] Yozu R, Golding L, Yada I, Harasaki H, Takatani S, Kawada S, et al. Do we really need pulse? chronic nonpulsatile and pulsatile blood flow: from the exercise response viewpoints. Artif Organs 1994;18(9):638–42.
[9] Baba A, Dobsak P, Mochizuki S, Saito I, Isoyama T, Takiura K, et al. Evaluation of pulsatile and nonpulsatile flow in microvessels of the bulbar conjunctiva in the goat with an undulation pump artificial heart. Artif Organs 2003;27 (10):875–81.
[10] Ishbulatov YM, Kiselev AR, Mureeva EN, Popova YV, Kurbako AV, Gridnev VI, et al. Diagnostics of coupling between low-frequency loops in cardiovascular autonomic control in adults, newborns and mathematical model using cross-recurrence analysis. Russ Open Med J 2019;8(4):1–5.
[11] Karavaev A, Ishbulatov YM, Ponomarenko V, Bezruchko B, Kiselev A, Prokhorov M. Autonomic control is a source of dynamical chaos in the cardiovascular system. Chaos 2019;29(12):121101.

[12] Seidel H, Herzel H. Bifurcations in a nonlinear model of the baroreceptor-cardiac reflex. Phys D: Nonlinear Phenom 1998;115(1-2):145–60.
[13] Kotani K, Struzik ZR, Takamasu K, Stanley HE, Yamamoto Y. Model for complex heart rate dynamics in health and diseases. Phys Rev E 2005;72(4):041904.
[14] Bighamian R, Parvinian B, Scully CG, Kramer G, Hahn J-O. Control-oriented physiological modeling of hemodynamic responses to blood volume perturbation. Control Eng Pract 2018;73:149–60.
[15] Ursino M. Interaction between carotid baroregulation and the pulsating heart: a mathematical model. Am J Physiol-Heart Circ Physiol 1998;275(5):H1733–47.
[16] Ursino M, Fiorenzi A, Belardinelli E. The role of pressure pulsatility in the carotid baroreflex control: a computer simulation study. Comput Biol Med 1996;26(4):297–314.
[17] Preiss G, Polosa C. Patterns of sympathetic neuron activity associated with Mayer waves. Am J Physiol-Legacy Content 1974;226(3):724–30.
[18] Ringwood JV, Kinnane OP. Prediction of low frequency blood pressure oscillations via a combined heart/resistance model. IFAC Proc Vol 2005;38(1):60–5.
[19] Ringwood JV, Taussi F, de Paor AM. The effect of pulsatile blood flow on blood pressure regulatory mechanisms. 2012 IEEE International Conference on Control Applications; 2012. pp. 609–14.
[20] Bagnall Hare H, Ringwood JV. The modulation of neural blood pressure control by blood pressure pulsatility. 2019 30th Irish Signals and Systems Conference (ISSC); 2019. pp. 1–6.
[21] Janssen B, Malpas SC, Burke SL, Head GA. Frequency-dependent modulation of renal blood flow by renal nerve activity in conscious rabbits. Am J Physiol – Regul Integr Comp Physiol 1997;273(2):R597–608.
[22] Osborn JW. Hypothesis: set-points and long-term control of arterial pressure. a theoretical argument for a long-term arterial pressure control system in the brain rather than the kidney. Clin Exp Pharmacol Physiol 2005;32(5–6):384–93.
[23] Thomas GD. Neural control of the circulation. Adv Physiol Educ 2011;35(1):28–32.
[24] Burattini R, Natalucci S. Complex and frequency-dependent compliance of viscoelastic W indkessel resolves contradictions in elastic W indkessels. Med Eng Phys 1998;20(7):502–14.
[25] Ikeda Y, Kawada T, Sugimachi M, Kawaguchi O, Shishido T, Sato T, et al. Neural arc of baroreflex optimizes dynamic pressure regulation in achieving both stability and quickness. Am J Physiol-Heart Circ Physiol 1996;271(3): H882–90.
[26] Kawada T, Zheng C, Yanagiya Y, Uemura K, Miyamoto T, Inagaki M, et al. High-cut characteristics of the baroreflex neural arc preserve baroreflex gain against pulsatile pressure. Am J Physiol-Heart Circ Physiol 2002;282(3): H1149–56.
[27] de Paor A, Ringwood J. A simple soft limiter describing function for biomedical applications. IEEE Trans Biomed Eng 2006;53(7):1233–40.
[28] Sato T, Kawada T, Inagaki M, Shishido T, Takaki H, Sugimachi M, et al. New analytic framework for understanding sympathetic baroreflex control of arterial pressure. Am J Physiol-Heart Circ Physiol 1999;276(6): H2251–6.
[29] Levy MN. Sympathetic-parasympathetic interactions in the heart. Circ Res 1971;29(5):437–45.
[30] Seidel H. Nonlinear dynamics of physiological rhythms. Lagos Verlag; 1997.
[31] Kawada T, Sugimachi M, Shishido T, Miyano H, Sato T, Yoshimura R, et al. Simultaneous identification of static and dynamic vagosympathetic interactions in regulating heart rate. Am J Physiol – Regul Integr Comp Physiol 1999;276(3):R782–9.
[32] Barrett CJ, Ramchandra R, Guild S-J, Lala A, Budgett DM, Malpas SC. What sets the long-term level of renal sympathetic nerve activity: a role for Angiotensin II and baroreflexes? Circ Res 2003;92(12):1330–6.
[33] 1926 Association for the Publication of the Journal of Internal Medicine, Part II: The heart's minute-volume and stroke-volume in rabbits in normal condition and during experimental pneumonia. J Intern Med 1926;64(s17):60–182.
[34] Guild S-J, Austin PC, Navakatikyan M, Ringwood JV, Malpas SC.Dynamic relationship between sympathetic nerve activity and renal blood flow: a frequency domain approach. Am J Physiol – Regul Integr Comp Physiol 2001;281(1):R206–12.
[35] Siddiqui A.Effects of vasodilation and arterial resistance on cardiac output. J Clin Exp Cardiol 2011;2(11).
[36] Simpson R, Power H.Applications of high frequency signal injection in non-linear systems. Int J Control 1977;26 (6):917–43.
[37] Guild S-J. Private communication; 2018.
[38] Atherton DP. Nonlinear control engineering. Van Nostrand Reinhold Company; 1975.
[39] Moré JJ. The Levenberg-Marquardt algorithm: implementation and theory. Numerical analysis. Springer; 1978. p. 105–16.
[40] Coleman TF, Li Y.An interior trust region approach for nonlinear minimization subject to bounds. SIAM J Optim 1996;6(2):418–45.
[41] Lagarias JC, Reeds JA, Wright MH, Wright PE.Convergence properties of the nelder-mead simplex method in low dimensions. SIAM J Optim 1998;9(1):112–47.
[42] Malpas SC, Bendle RD, Head GA, Ricketts JH.Frequency and amplitude of sympathetic discharges by baroreflexes during hypoxia in conscious rabbits. Am J Physiol – Heart Circ Physiol 1996;271(6):H2563–74.
[43] Malpas SC, Evans RG, Head GA, Lukoshkova EV. Contribution of renal nerves to renal blood flow variability during hemorrhage. Am J Physiol – Regul Integr Comp Physiol 1998;274(5):R1283–94.
[44] Liu H-K, Guild S-J, Ringwood JV, Barrett CJ, Leonard BL, Nguang S-K, et al. Dynamic baroreflex control of blood pressure: influence of the heart vs. peripheral resistance. Am J Physiol – Regul Integr Comp Physiol 2002;283(2):R533–42.